Hindawi
International Journal of Antennas and Propagation
Volume 2021, Article ID 8871255, 16 pages
https://doi.org/10.1155/2021/8871255

Research Article

Analytical Nonstationary 3D MIMO Channel Model for Vehicle-to-Vehicle Communication on Slope

Kaizhen Liu, Zaixue Wei, and Sibo Chen

School of Information and Telecommunication Engineering, Beijing University of Posts and Telecommunications, Beijing 100876, China

Correspondence should be addressed to Zaixue Wei; zaixuew@bupt.edu.cn

Received 2 October 2020; Revised 18 December 2020; Accepted 23 December 2020; Published 13 January 2021

Academic Editor: Shah Nawaz Burokur

Vehicle-to-vehicle communication plays a strong role in modern wireless communication systems, appropriate channel models are of great importance in future research, and propagation environment with slope is one special kind. In this study, a novel three-dimensional nonstationary multiple-input multiple-output channel model for the sub-6 GHz band is proposed. This model is a regular-shaped multicluster geometry-based analytical model, and it combines the line-of-sight component and multicluster scattering rays as the nonline-of-sight components. Each cluster of scatterers represents the influence of different moving vehicles on or near a slope, and scatterers are, respectively, distributed within two spheres around the transmitter and the receiver. In this model, it is considered that the azimuth and elevation angles of departure and arrival are jointly distributed and conform to the von Mises–Fisher distribution, which can easily control the range and concentration of the scatterers within spheres to mimic the real-world situation well. Moreover, the impulse response and the autocorrelation function of the corresponding channel is derived and proposed; then, the Doppler power spectrum density of the channel is simulated and analyzed. In addition, the nonstationary characteristics of the presented channel model are observed through simulations. Finally, the simulation results are compared with measurement data in order to validate the utility of the proposed model.

1. Introduction

In recent years, the applications of vehicle-to-vehicle (V2V) communications have become more extensive and valuable, such as vehicular networking [1–3], the cooperative vehicular system [4], and intelligent transportation [5]. Besides, the accuracy of performance evaluation for V2V communications is to some extent determined by precise modeling of the channel. Reference [6] analyzed vehicular communications from the physical layer. With the mature multiple-input multiple-output (MIMO) technology [7, 8], the performance of V2V communications has been greatly improved. Compared to other communication scenarios, V2V communications have their unique characteristics, i.e., both the transmitter (Tx) and the receiver (Rx) are in high-speed movements, the shapes and heights of different vehicles are similar, and the heights of vehicles are generally between one and two meters, so vehicles usually have antennas with low elevation angles. Thus, the obstruction of the slope will affect the performance of V2V communication seriously. With these special features, the channel modeling of V2V communications is essential and necessary, especially the propagation model on slope terrain. The path loss for V2V scenario with slope has been studied in several works. References [9, 10] proposed path loss prediction models for slope terrain in small-sized cells. However, research on the modeling of scatterers still needs to be finished.

The modeling of V2V channels can be of great help in testing the performance and properties of V2V channels. Reference [11] presented propagation models for urban environment. Besides, several precise channel models for other scenarios have been proposed by other researchers. According to this literature, channel models can generally be classified into deterministic models and stochastic models. Stochastic models are further categorized as geometry-based stochastic models (GBSMs) [12] and nongeometry-based

stochastic models (NGBSMs) [13]. GBSMs assume that scatterers are distributed on a certain geometry and use methods similar to ray-tracing to represent scattering rays. In further classification, GBSMs can be categorized as regular-shaped GBSMs (RS-GBSMs) [14] and irregular-shaped GBSMs (IS-GBSMs) [15]. RS-GBSMs assume that these geometries are regular shapes, e.g., sphere, ring, or cylinder. In other ways, GBSMs can be divided into two-dimensional (2D) GBSMs [16] and three-dimensional (3D) GBSMs [17] according to the dimension of models. Considering the pattern of antenna arrays, the models can be categorized as single-input single-output (SISO) models [18] and MIMO models [19]. Additionally, in [20], a 3D model adopting massive-MIMO technology was proposed.

Comparisons with measurements [21–23] showed that GBSMs could be applied to V2V channel modeling suitably. V2V channels were modeled in 2D due to the very narrow elevation angle of the vehicle antennas at the early time. In [24], the authors proposed a nonstationary 2D RS-GBSM consisting of multiple confocal ellipses for high-mobility intelligent transportation systems. In [25], a 2D RS-GBSM with two-ring for a nonisotropic scattering environment was proposed. Furthermore, 2D models were extended to 3D models because they could better simulate the realistic propagation environment, e.g., the 2D two-circular RS-GBSM [25] was updated to the 3D two-cylinder RS-GBSM in [26], and the 2D two-circular and one-ellipse RS-GBSM [27] was extended to the 3D two-sphere and one-ellipse-cylinder RS-GBSM in [28]. Including the above listed, 3D GBSMs can be classified according to the geometries of scattering, such as spheres, cylinders, one/two semiellipsoid [29–31], and one/two hollow semiellipsoid around the Tx/Rx [32, 33]. In addition, GBSMs can be divided into stationary GBSMs and nonstationary GBSMs [34–42]. The nonstationary GBSMs are closer to reality due to the time-varying parameters of the V2V channel. According to the abovementioned literature, it can be noticed that in the RS-GBSM based channel modeling, the modeling of the scatterer distribution is crucial. In RS-GBSM-based models, isotropic and nonisotropic distributions of scatterers are considered, and the latter is more reasonable. In [27, 35, 36, 43], von Mises distributions were adopted to model the distributions of the scatterers in 2D modeling as nonisotropic models. In [28, 37, 44–48], 3D nonisotropic distributions of scatterers were modeled with von Mises–Fisher (VMF) distributions. By now, the VMF distribution is perhaps the most suitable distribution for 3D nonisotropic scattering modeling.

In the aforementioned literature, although nonisotropic 3D scatterers have been modeled, scatterers were always assumed to be concentrated in the direction of the line-of-sight (LoS) path. Further discussions on multidirection scatterers modeling should be conducted. Besides, limited specific models are for vehicles near or on a slope as well as overtaking cases.

The motivation of this research is to present a flexible 3D nonstationary V2V channel model with multidirection distributing scatterers on or near slope terrain. Based on the two-sphere 3D RS-GBSM V2V nonstationary models in [28, 37, 48, 49], we abandoned the additional elliptical cylinder and introduced multidirection scattering clusters to model the multidirectional isotropic scatterers. More distinctly, in the model we proposed, rays are scattered by other vehicles in several directions in the form of cluster around Tx and Rx. This is the major difference between our model and [28, 49, 50] and basic theories found in [51]. For the modeling of nonisotropic scattering, the elevation and azimuth angles of arrival (AoAs) and the elevation and azimuth angles of departure (AoDs) are jointly distributed and subjected to VMF distribution, as in [45, 47]. Finally, we compare the simulation results with the measurement data.

In summary, the main contributions of this study are as follows:

(1) A nonstationary 3D V2V MIMO RS-GBSM is proposed, which is applied to the scenario where Tx and Rx are surrounded by multiple vehicles on slope, and the vehicle can change lanes or overtake during the movement. The statistical properties of this MIMO channel model are derived and analyzed.

(2) The nonstationary characteristics of the proposed model are derived and simulated. The simulation results support the utility of the model.

(3) The proposed model is compared with the measurement data in four different communication scenarios. The comparisons include root mean square (RMS) delay spread, RMS Doppler spread, and root mean squared error (RMSE).

The rest of this study is arranged as follows. Section 2 gives detailed definition of the model. The expression of channel impulse response (CIR) is given in Section 3. In Section 4, the statistical properties are calculated. Section 5 is the simulation results and the comparison with measurement data. The conclusion is presented in Section 6.

Notation: the superscript $(\cdot)^T$ denotes the transpose operator. The superscript $(\cdot)^*$ denotes the conjugate operator. $|x|$ is the norm of a vector x. $\mathbb{E}\{\cdot\}$ denotes the expectation operator. $p(\alpha, \beta)$ is the probability density function (PDF) of the VMF distribution with parameters α and β.

2. Nonstationary 3D RS-GBSM for V2V MIMO Channels

The presented 3D RS-GBSM is for MIMO V2V communication systems, and the system structure is shown in Figures 1 and 2. We assume that both of Tx and Rx are surrounded by several vehicles. For convenience on building the coordinates, we assume that Tx follows Rx, and it can be very easily adapted to other cases. The coordinates are as shown in Figure 2. According to the different positions of Tx and Rx on the slope, it can be divided into 2 scenarios: (1) all vehicles are on the slope; (2) Tx and surrounding vehicles are off the slope and moving towards the bottom end of the slope while Rx and surrounding vehicles are on the slope.

2.1. Model Specific Description. The distribution of scatterers in the multicluster form at the Tx side is shown in Figure 3. Since the distribution of scatterers at the Rx side is the same

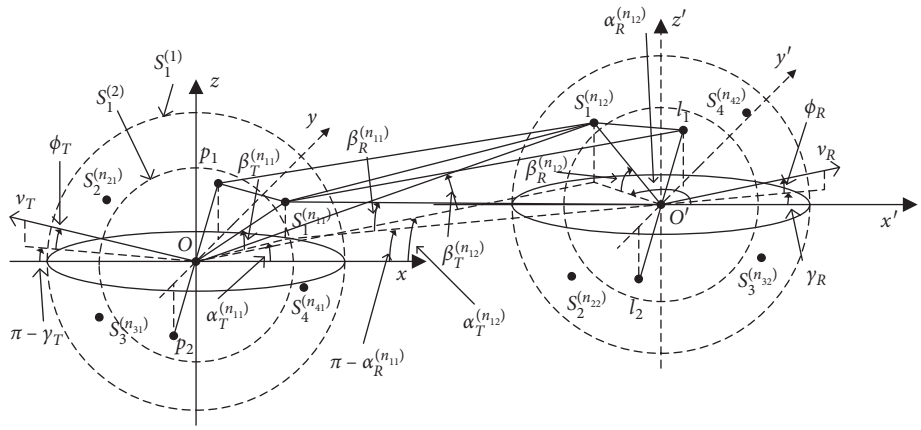

Figure 1: The proposed 3D RS-GBSM for V2V MIMO channels at $t = 0$ s.

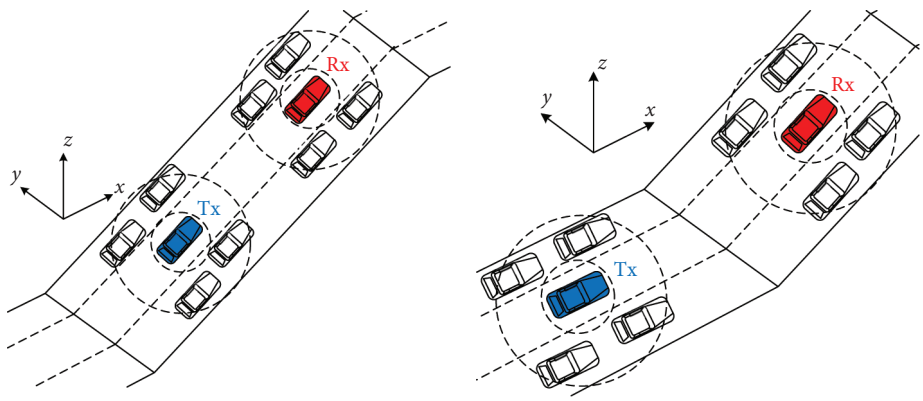

Figure 2: The real scenario of the 3D RS-GBSM. (a) Scenario 1 and (b) scenario 2.

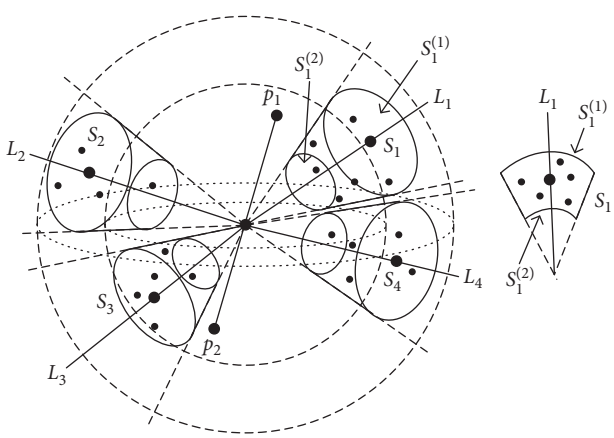

Figure 3: The detailed distribution of scatterers on the Tx sphere. The distribution of scatterers near Rx is consistent with Tx.

as the Tx side, we only illustrate the Tx side. Taking cluster S_1 as an example, the scatterers are distributed around the main path L_1 and obeying the VMF distribution. Since vehicles have a certain volume, the radii of different scatterers to Tx and Rx are different. Limited by the radii, they are distributed between $s_1^{(1)}$ and $s_1^{(2)}$, i.e., all scatterers are distributed within the outermost and innermost two spheres. For clearer description of the structure, the concerned paths and parameters are shown in Figure 1. Major parameters in this study are listed in Table 1. According to the realistic situation, both the LoS and non-LoS (NLoS) components are included. A two-sphere model is developed for the NLoS components. As shown in Figures 1 and 3, effective scatterers are distributed between two spheres, and they are distributed in the form of clusters. Taking the four-cluster scenario as an example, there are four clusters of scatterers at both ends of Tx and Rx, representing, respectively, four vehicles around Tx and Rx, and scatterers are distributed on the surface and in these vehicles. As mentioned above, each effective scatterer has a different radius, and the specific way of modeling is shown in Figure 3. In Figure 1, we assume that both of Tx and Rx are equipped with multiple antennas. The antenna elements are omnidirectional, and the numbers of antennas at Tx and Rx are denoted as n_t and n_r, respectively. In this model, taking 2×2 MIMO as an example, the two antennas of the Tx are labeled p_1 and p_2, and the two antennas of the Rx are labeled l_1 and l_2. In addition, we consider that both Tx and Rx are moving at high speeds, and the directions of the movements of the Tx and Rx are jointly defined by elevation angles and azimuth

Table 1: Definition and unit of key parameters in model.

Parameters	Definitions	Units
f_c	Central frequency	Hz
$D(t)$	Distance between Tx and Rx in scenario 1	m
$D_1(t)$	Distance between Tx and the bottom end of slope in scenario 2	m
$D_2(t)$	Distance between the bottom end of slope and Rx in scenario 2	m
$R_T(t), R_R(t)$	The radius of Tx and Rx spheres	m
δ_T, δ_R	The antenna elements spacing at Tx and Rx	m
$v_T(t), v_R(t)$	Velocity vectors of Tx and Rx	m/s
$v_{\text{scatterer}}(t)$	Velocity vectors of vehicles around Tx and Rx	m/s
$\phi_T(t), \phi_R(t)$	The elevation angles of movement direction of Tx and Rx	rad
$\gamma_T(t), \gamma_R(t)$	The azimuth angles of movement direction of Tx and Rx	rad
$f_{T_{\max}}(t), f_{R_{\max}}(t)$	The maximum Doppler shifts caused by Tx and Rx	Hz
$f_{T_{\text{Doppler}}}(t), f_{R_{\text{Doppler}}}(t)$	The Doppler shifts caused by Tx and Rx	Hz
$\theta_T(t), \theta_R(t)$	The horizontal orientation of antenna array of Tx and Rx	rad
$\alpha_{T_{\{n_{ij}\}}}(t)$	The AAoD at $S_i^{(n_{ij})}$	rad
$\alpha_{R_{\{n_{ij}\}}}(t)$	The AAoA from $S_i^{(n_{ij})}$	rad
$\beta_{T_{\{n_{ij}\}}}(t)$	The EAoD at $S_i^{(n_{ij})}$	rad
$\beta_{R_{\{n_{ij}\}}}(t)$	The EAoA from $S_i^{(n_{ij})}$	rad
$\alpha_T^{\text{LoS}}(t), \beta_T^{\text{LoS}}(t)$	The AAoD and EAoD of the LoS path	rad
$\alpha_R^{\text{LoS}}(t), \beta_R^{\text{LoS}}(t)$	The AAoA and EAoA of the LoS path	rad
$d(S_1, S_2)(t)$	The distance between S_1 and S_2	m
N_c	The number of vehicles (clusters) around Tx and Rx	
N_{i_1}, N_{i_2}	The number of scatterers in the ith cluster on the Tx/Rx sphere	
θ_{slope}	The tilt angle of the slope	rad

angles. The azimuth and elevation angles of the movement directions are recorded as $\gamma_T(t), \gamma_R(t), \phi_T(t)$, and $\phi_R(t)$, and the velocities of the movements are recorded with $v_T(t)$and $v_R(t)$. As mentioned before, the effective scatterers are distributed over a section of the sphere and are distributed in the form of clusters, denoted by $S_i^{n_{ij}}$ ($i = 1, \ldots, N_c$ and $j = 1, 2$), where i represents that the scatterers are located in the ith cluster, $j = 1$ represents that the scatterers are on the Tx sphere, and $j = 2$ represents that the scatterers are on the Rx sphere. In the ith cluster, n_{ij} represents that the scatterer is the $n_{ij}{}^{\text{th}}$ scatterer of this cluster. $\alpha_T^{n_{ij}}(t)$ and $\beta_T^{n_{ij}}(t)$ are the azimuth AoD (AAoD) and elevation AoD (EAoD) of the path. $\alpha_R^{n_{ij}}(t)$ and $\beta_R^{n_{ij}}(t)$ are the azimuth AoA (AAoA) and elevation AoA (EAoA) of the path. The scattering paths can be divided into three types: (1) rays that are only reflected once at the Tx end, and these paths are called L^{SB_1}. (2) Rays that are only reflected once at the Rx end, and these paths are called L^{SB_2}. (3) Rays that are reflected twice at both of the Tx and Rx ends, and these paths are called L^{DB}. With the distances between adjacent antennas δ_T and δ_R and the radii of the two spheres R_T and R_R, we have $\delta_T, \delta_R \ll R_T, R_R$.

2.2. Vehicle Trajectory. We have considered not only the situation where vehicles move in a straight line but also the situation where one vehicle changes lane or overtakes. Vehicle's trajectory is shown in Figure 4. The initial time and final time are recorded as t_{ini} and t_{fin}. The location, velocity, and acceleration of the vehicle in the X-axis and Y-axis directions at the initial time and the final time are recorded as ($x_{\text{ini}}, \dot{x}_{\text{ini}}, \ddot{x}_{\text{ini}}, y_{\text{ini}}, \dot{y}_{\text{ini}}, \ddot{y}_{\text{ini}}$) and ($x_{\text{fin}}, \dot{x}_{\text{fin}}, \ddot{x}_{\text{fin}}, y_{\text{fin}}, \dot{y}_{\text{fin}}, \ddot{y}_{\text{fin}}$); x, $\dot{x}$, and $\ddot{x}$ denote distance, velocity, and acceleration, respectively.

We define the location of the vehicle in the X-axis and the Y-axis direction as

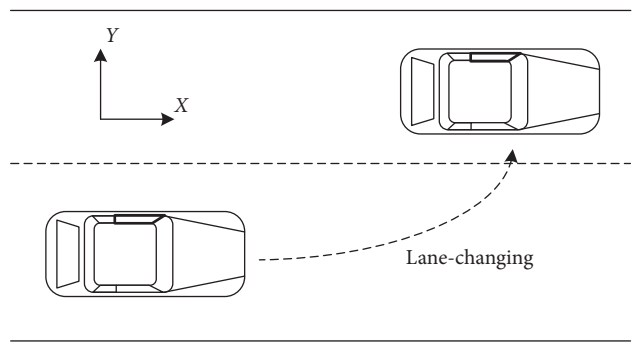

Figure 4: Vehicle lane-changing trajectory.

$$x(t) = a_5 t^5 + a_4 t^4 + a_3 t^3 + a_2 t^2 + a_1 t + a_0, \tag{1a}$$

$$y(t) = b_5 t^5 + b_4 t^4 + b_3 t^3 + b_2 t^2 + b_1 t + b_0. \tag{1b}$$

Then, we let $A = [\, a_5 \;\; a_4 \;\; a_3 \;\; a_2 \;\; a_1 \;\; a_0 \,]$, $B = [\, b_5 \;\; b_4 \;\; b_3 \;\; b_2 \;\; b_1 \;\; b_0 \,]$, and we define the time parameter matrix:

$$T_{6\times 6} = \begin{bmatrix} t_{\text{ini}}^5 & t_{\text{ini}}^4 & t_{\text{ini}}^3 & t_{\text{ini}}^2 & t & 1 \\ 5t_{\text{ini}}^4 & 4t_{\text{ini}}^3 & 3t_{\text{ini}}^2 & 2t_{\text{ini}} & 1 & 0 \\ 20t_{\text{ini}}^3 & 12t_{\text{ini}}^2 & 6t_{\text{ini}} & 2 & 0 & 0 \\ t_{\text{fin}}^5 & t_{\text{fin}}^4 & t_{\text{fin}}^3 & t_{\text{fin}}^2 & t_{\text{fin}} & 1 \\ 5t_{\text{fin}}^4 & 4t_{\text{fin}}^3 & 3t_{\text{fin}}^2 & t_{\text{fin}} & 1 & 0 \\ 20t_{\text{fin}}^3 & 12t_{\text{fin}}^2 & 6t_{\text{fin}} & 2 & 0 & 0 \end{bmatrix}. \tag{2}$$

Now, we obtain

$$\left[\, x_{\text{ini}} \;\; \dot{x}_{\text{ini}} \;\; \ddot{x}_{\text{ini}} \;\; x_{\text{fin}} \;\; \dot{x}_{\text{fin}} \;\; \ddot{x}_{\text{fin}} \,\right]^T = T_{6\times 6} \cdot A^T, \tag{3a}$$

$$\left[\, y_{\text{ini}} \;\; \dot{y}_{\text{ini}} \;\; \ddot{y}_{\text{ini}} \;\; y_{\text{fin}} \;\; \dot{y}_{\text{fin}} \;\; \ddot{y}_{\text{fin}} \,\right]^T = T_{6\times 6} \cdot B^T. \tag{3b}$$

Finally, the solution of the inhomogeneous linear equations (3a) and (3b) can be derived through the boundary conditions. Using this method, we can quickly obtain the track of vehicle's overtaking or lane-changing. However, the trajectory does not consider the dynamic characteristics of the vehicle, and the generated acceleration should be limited by the condition of vehicle engine, tire, ground friction, and other restrictions. Commonly, we have $-2.5\,\text{m/s}^2 < \ddot{x} < 2.5\,\text{m/s}^2$ and $2\,\text{m/s}^2 < \ddot{y} < 2\,\text{m/s}^2$.

3. Channel Impulse Response

In this section, the detailed deduction of the CIR is given. Take path $p_1 \longrightarrow l_1$ as an example. Since scenario 1 and scenario 2 are very similar in derivation, we only give the derivation process for scenario 1. The CIR can be divided into three parts: LoS, single-bounced (SB), and double-bounced (DB) components. Then, the CIR can be expressed as

$$h_{p_1 l_1}(t) = h_{\text{LoS}}(t) + \sum_{i=1}^{2} h_{p_1 l_1}^{\text{SB}_i}(t) + h_{p_1 l_1}^{\text{DB}}(t). \tag{4}$$

The Doppler shift caused by the Tx's motion is

$$\begin{aligned} f_{T_{\text{Doppler}}}(t) = {} & f_{T_{\max}}(t)\,(\cos\beta_T(t)\cos\alpha_T(t)\cos\phi_T(t)\cos\gamma_T(t) \\ & + \cos\beta_T(t)\sin\alpha_T(t)\cos\phi_T(t)\sin\gamma_T(t) \\ & + \sin\beta_T(t)\sin\phi_T(t)). \end{aligned} \tag{5a}$$

Correspondingly, the Doppler shift caused by the Rx's motion can be expressed as

$$\begin{aligned} f_{R_{\text{Doppler}}}(t) = {} & f_{R_{\max}}(t)\,(\cos\beta_R(t)\cos\alpha_R(t)\cos\phi_R(t)\cos\gamma_R(t) \\ & + \cos\beta_R(t)\sin\alpha_R(t)\cos\phi_R(t)\sin\gamma_R(t) \\ & + \sin\beta_R(t)\sin\phi_R(t)), \end{aligned} \tag{5b}$$

where $f_{T_{\max}}(t) = |v_T(t)|/\lambda$ and $f_{R_{\max}}(t) = |v_R(t)|/\lambda$ are the maximum Doppler shifts at time t, λ is the carrier wavelength, and $v_T(t)$ and $v_R(t)$ are the velocity vectors of the Tx and Rx.

Then, the three parts of the CIR can be rewritten as

$$h_{p_1 l_1}^{\text{LoS}}(t) = \sqrt{\frac{K}{K+1}}\, e^{-j(2\pi/\lambda)d(p_1,l_1)(t)} \times e^{j2\pi f_{T_{\text{Doppler}}}^{\text{LoS}}(t)t}\, e^{j2\pi f_{R_{\text{Doppler}}}^{\text{LoS}}(t)t}, \tag{6a}$$

$$\begin{aligned} h_{p_1 l_1}^{\text{SB}_i}(t) = {} & \sqrt{\frac{1}{K+1}}\,\varepsilon_{\text{SB}_i} \lim_{N_i \longrightarrow \infty} \sum_{k=1}^{N_c} \sum_{n_{ki}=1}^{N_{ki}} \frac{1}{\sqrt{N_i}} \\ & \times e^{j\left\{\psi_{n_{ki}} - (2\pi/\lambda)\left[d\left(p_1, S_k^{(n_{ki})}\right)(t) + d\left(S_k^{(n_{ki})}, l_1\right)(t)\right]\right\}} \\ & \times e^{j2\pi f_{T_{\text{Doppler}}}^{\text{SB}_i}(t)t}\, e^{j2\pi f_{R_{\text{Doppler}}}^{\text{SB}_i}(t)t}, \end{aligned} \tag{6b}$$

$$\begin{aligned} h_{p_1 l_1}^{\text{DB}}(t) = {} & \sqrt{\frac{1}{K+1}}\,\varepsilon_{\text{DB}} \lim_{N_1, N_2 \longrightarrow \infty} \sum_{i,k=1}^{N_c} \sum_{n_{i1}, n_{k2}=1}^{N_{i1}, N_{k2}} \frac{1}{\sqrt{N_1 N_2}} \\ & \times e^{j\left[\psi_{n_{i1}, n_{k2}} - (2\pi/\lambda)\right) d_{\text{DB}}(t)]} \\ & \times e^{j2\pi f_{T_{\text{Doppler}}}^{DB}(t)t}\, e^{j2\pi f_{R_{\text{Doppler}}}^{DB}(t)t}, \end{aligned} \tag{6c}$$

where N_{i1} is the number of effective scatterers in the ith cluster on the Tx sphere, N_{i_2} is the number of effective scatterers in the ith cluster on the Rx sphere, $N_1 = \sum_{i=1}^{N_c} N_{i_1}$, $N_2 = \sum_{i=1}^{N_c} N_{i_2}$, $d_{\text{DB}}(t) = d(p_1, S_i^{(n_{i_1})})(t) + d(S_i^{(n_{i_1})}, S_k^{(n_{k_2})})(t) + d(S_k^{(n_{k_2})}, l_1)(t)$, $j^2 = -1$, K is the Ricean factor, and SB_1, SB_2, and DB, respectively, represent L^{SB_1}, L^{SB_2}, and L^{DB} which have been introduced in Section 2. Parameters $\varepsilon_{\text{SB}_i}$ and ε_{DB} are related to the power of different paths, they control the proportions of power among paths L^{SB_1}, L^{SB_2}, and L^{DB}, and they satisfy $\varepsilon_{\text{SB}_1}^2 + \varepsilon_{\text{SB}_2}^2 + \varepsilon_{\text{DB}}^2 = 1$. $\psi_{n_{ki}}$ and $\psi_{n_{i_1}, n_{k_2}}$ are the random phases, and they are uniformly distributed within $[-\pi, \pi)$. $f_{T/R_{\text{Doppler}}}^{\text{LoS/SB}_i/\text{DB}}(t)$, respectively, represent the Doppler shifts at Tx and Rx of the LoS, SB, and DB components. The expressions are derived as (5a) and (5b). For LoS component, $\alpha_{T/R}(t) = \alpha_{T/R}^{\text{LoS}}(t)$ and $\beta_{T/R}(t) = \beta_{T/R}^{\text{LoS}}(t)$. In terms of SB and DB components, we have $\alpha_{T/R}(t) = \alpha_{T/R}^{(n_{ij})}(t)$ and $\beta_{T/R}(t) = \beta_{T/R}^{(n_{ij})}(t)$.

We consider that the locations of Tx and Rx are known through the global positioning system; the location of p_1 is $[x_{p_1}(t), y_{p_1}(t), z_{p_1}(t)]$, and the location of l_1 is $[x_{l_1}(t), y_{l_1}(t), z_{l_1}(t)]$. In scenario 1, Tx, Rx, and surrounding vehicles are constantly moving on the slope. At initial time, $x_{p_1}(t) = 0$, $y_{p_1}(t) = \delta_T \cos\theta_T(t)/2$, $z_{p_1}(t) = \delta_T \sin\theta_T(t)/2$, $x_{l_1} = D(t)\cos\theta_{\text{slope}}$, $y_{l_1}(t) = \delta_R \cos\theta_R(t)/2$, and $z_{l_1}(t) = \delta_R \sin\theta_R(t)\sin\theta_{\text{slope}}/2$. The location of $S_i^{(n_{i_1})}$ can be denoted as $[x_{s_1}(t), y_{s_1}(t), z_{s_1}(t)]$:

$$x_{s_1}(t) = R_T(t)\cos\beta_T^{\left(n_{i_1}\right)}(t)\cos\alpha_T^{\left(n_{i_1}\right)}(t), \tag{7a}$$

$$y_{s_1}(t) = R_T(t)\cos\beta_T^{\left(n_{i_1}\right)}(t)\sin\alpha_T^{\left(n_{i_1}\right)}(t), \tag{7b}$$

$$z_{s_1}(t) = R_T(t)\sin\beta_T^{\left(n_{i_1}\right)}(t). \tag{7c}$$

The location of $S_i^{(n_{i2})}$ is denoted as $[x_{s_2}(t), y_{s_2}(t), z_{s_2}(t)]$ and

$$\begin{aligned} x_{s_2}(t) = {} & R_R(t)\cos\beta_R^{\left(n_{i_2}\right)}(t)\cos\alpha_R^{\left(n_{i_2}\right)}(t) \\ & + D(t)\cos\theta_{\text{slope}}, \end{aligned} \tag{8a}$$

$$y_{s_2}(t) = R_R(t)\cos\beta_R^{\left(n_{i_2}\right)}(t)\sin\alpha_R^{\left(n_{i_2}\right)}(t), \tag{8b}$$

$$\begin{aligned} z_{s_2}(t) \approx {} & \left(D(t)\cos\theta_{\text{slope}} + R_R(t)\cos\alpha_R^{\left(n_{i_2}\right)}(t)\right) \\ & \times \tan\theta_{\text{slope}} + R_R(t)\sin\beta_R^{\left(n_{i_2}\right)}(t). \end{aligned} \tag{8c}$$

Then, we can easily calculate $d(p_1, l_1)(t)$, $d(p_1, S_i^{(n_{i_1})})(t)$, $d(S_j^{(n_{j_2})}, l_1)(t)$, and $d(S_i^{(n_{i_1})}, S_j^{(n_{j_2})})(t)$; take $d(p_1, l_1)(t)$, for example, we have

$$\begin{aligned} & d(p_1, l_1)(t) \\ & = \sqrt{\Delta x_{l_1 p_1}^2(t) + \Delta y_{l_1 p_1}^2(t) + \Delta z_{l_1 p_1}^2(t)} \\ & = \sqrt{\left(D(t)\cos\theta_{\text{slope}}\right)^2 + \left[\frac{(\delta_R \cos\theta_R(t) - \delta_T \cos\theta_T(t))}{2}\right]^2 + \left[\frac{\left(\delta_R \sin\theta_R(t)\sin\theta_{\text{slope}} - \delta_T \sin\theta_T(t)\right)}{2}\right]^2}. \end{aligned} \tag{9}$$

In DB paths, EAoD/AAoD and EAoA/AAoA are independent, whereas in SB_1 and SB_2 paths, they are related. The generation of angles is introduced in Section 4.

4. Space-Time Correlation Function and Doppler Power Spectrum Density

4.1. Space-Time Correlation Function. The normalized space-time correlation function (STCF) between path $p_1 \longrightarrow l_1$ and $p_2 \longrightarrow l_2$ is defined as

$$\begin{aligned} & R_{p_1 l_1, p_2 l_2}(\delta_T, \delta_R, t, \tau) \\ & = \frac{\mathbb{E}\left\{h_{p_1 l_1}(t) h_{p_2 l_2}^*(t+\tau)\right\}}{\sqrt{\mathbb{E}\left\{\left|h_{p_1 l_1}(t)\right|^2\right\}\mathbb{E}\left\{\left|h_{p_2 l_2}(t)\right|^2\right\}}} = (K+1)\mathbb{E}\left\{h_{p_1 l_1}(t) h_{p_2 l_2}^*(t+\tau)\right\}. \end{aligned} \tag{10}$$

The STCF can be written into

$$R_{p_1 l_1, p_2 l_2}(\delta_T, \delta_R, t, \tau) = R_{p_1 l_1^{\text{LoS}}, p_2 l_2^{\text{LoS}}}(\delta_T, \delta_R, t, \tau) + \sum_{i=1}^{2} R_{p_1 l_1^{\text{SB}_i}, p_2 l_2^{\text{SB}_i}}(\delta_T, \delta_R, t, \tau) + R_{p_1 l_1^{\text{DB}}, p_2 l_2^{\text{DB}}}(\delta_T, \delta_R, t, \tau). \tag{11}$$

(a) STCF of LoS component: we also only give the derivation for scenario 1 because it is similar to the scenario 2. The STCF of the LoS component is

$$\begin{aligned} R_{l_1 p_1^{\text{LoS}}, l_2 p_2^{\text{LoS}}}(\delta_T, \delta_R, t, \tau) &= K e^{-j(2\pi/\lambda)\Delta d(t)} \times e^{j2\pi\tau\left(f_{T_{\text{Doppler}}}^{\text{LoS}}(t) + f_{R_{\text{Doppler}}}^{\text{LoS}}(t)\right)} \\ &= K e^{-j(2\pi/\lambda)\left(d(p_1, l_1)(t) + d(p_2, l_2)(t)\right)} \times e^{j2\pi\tau\left(f_{T_{\text{Doppler}}}^{\text{LoS}}(t) + f_{R_{\text{Doppler}}}^{\text{LoS}}(t)\right)}, \end{aligned} \tag{12}$$

where $d(p_1, l_1)(t)$ and $d(p_2, l_2)(t)$ can be calculated as (9). $f_{T_{\text{Doppler}}}^{\text{LoS}}(t)$ and $f_{R_{\text{Doppler}}}^{\text{LoS}}(t)$ have been expressed in Section 3.

(b) STCF of SB components: we consider that the EAoD and the AAoD in SB_1 and EAoA and AAoA in SB_2 are contributed to VMF contribution; thus, the general PDF of these angles is

$$p(\alpha, \beta) = \frac{k\cos\beta_0}{4\pi\sinh k} \times e^{k\cos\beta_0\cos\beta\cos(\alpha - \alpha_0) + \sin\beta_0\sin\beta}, \tag{13}$$

where $\alpha, \beta \in [-\pi, \pi)$, and $\alpha_0, \beta_0 \in [-\pi, \pi)$. Since there are N_c clusters of scatterers, there are also N_c groups of α_0 and β_0 corresponding to $p_i(\alpha, \beta)$ $(i = 1, \ldots, N_c)$. Next, if the number of the scatterers tends to infinity,

the discrete random variables $\alpha_{T/R}^{(n_{ij})}$ and $\beta_{T/R}^{(n_{ij})}$ can be replaced by continuous random variables $\alpha_{T/R}$ and $\beta_{T/R}$. Then, the STCF of SB_i component becomes

$$R_{p_1 l_1^{\mathrm{SB}_1}, p_2 l_2^{\mathrm{SB}_1}}(\delta_T, \delta_R, t, \tau) = \varepsilon_{\mathrm{SB}_i}^2 \sum_{k=1}^{N_c} \int_{-\pi}^{\pi} \int_{-\pi}^{\pi} \left[e^{-j(2\pi/\lambda)\Delta d(t)} \times e^{j2\pi\tau f_{T_{\mathrm{Doppler}}}^{\mathrm{SB}_i}(t)} \times e^{j2\pi\tau f_{R_{\mathrm{Doppler}}}^{\mathrm{SB}_i}(t)} \times p_k(\alpha_T, \beta_T) \right] \mathrm{d}\alpha_T \mathrm{d}\beta_T, \tag{14}$$

where $\Delta d(t) = d(p_1, S_k)(t) + d(S_k, l_1)(t) - d(p_2, S_k)(t) - d(S_k, l_2)(t)$, and the calculations are similar to (9).

(c) STCF of DB components:

$$R_{p_1 l_1^{\mathrm{DB}}, p_2 l_2^{\mathrm{DB}}}(\delta_T, \delta_R, t, \tau) = \varepsilon_{\mathrm{DB}}^2 \sum_{i=1}^{N_c} \sum_{k=1}^{N_c} \int_{-\pi}^{\pi} \int_{-\pi}^{\pi} \int_{-\pi}^{\pi} \int_{-\pi}^{\pi} \left[e^{-j(2\pi/\lambda)\Delta d} e^{j2\pi\tau f_{T_{\mathrm{Doppler}}}^{\mathrm{DB}}(t)} e^{j2\pi\tau f_{T_{\mathrm{Doppler}}}^{\mathrm{DB}}(t)} \times p_i(\alpha_T, \beta_T) p_k(\alpha_R, \beta_R) \right] \mathrm{d}\alpha_T \mathrm{d}\alpha_R \mathrm{d}\beta_T \mathrm{d}\beta_R, \tag{15}$$

where $\Delta d(t) = d(p_1, S_i^{(i1)})(t) + d(S_i^{(i1)}, S_k^{(k2)})(t) + d(S_k^{(k2)}, l_1)(t) - d(p_2, S_i^{(i1)})(t) - d(S_i^{(i1)}, S_k^{(k2)})(t) - d(S_k^{(k2)}, l_2)(t)$.

4.2. Doppler Power Spectrum Density. If we apply the Fourier transform to the space-time correlation function, then we can get the corresponding Doppler power spectrum density (PSD).

$$S_{p_1 l_1, p_2 l_2}(t, f) = F_\tau\left\{R_{p_1 l_1^{\mathrm{LoS}}, p_2 l_2^{\mathrm{LoS}}}(t, \tau)\right\} + \sum_{i=1}^{2} F_\tau\left\{R_{p_1 l_1^{\mathrm{SB}_i}, p_2 l_2^{\mathrm{SB}_i}}(t, \tau)\right\} + F_\tau\left\{R_{p_1 l_1^{\mathrm{DB}}, p_2 l_2^{\mathrm{DB}}}(t, \tau)\right\}. \tag{16}$$

5. Simulation Results and Analysis

In this section, several statistical characteristics of the proposed channel model are simulated and analyzed, including the spatial ACF, temporal ACF, and Doppler PSD. Based on measurement data in [28, 52] and measurement methods in [53–55], the simulation parameters at the initial time are set and listed in Table 2. As for the scenario with slope scenario 2 is chosen in simulations. Due to the energy of the scattering path is much smaller than that contained in the LoS path, the LoS path is ignored in the spatial and temporal ACFs simulation. Besides, since the above measurement campaigns are completed on common roads without slope, in CIR, time-varying ACF, and Doppler PSD simulations, the propagation scenario is reduced to a level load.

5.1. Simulation of CIR. As mentioned above, in the realistic scenario, the velocity and position vectors of the vehicle are constantly changing; thus, the nonstationary model is closer to reality. The tapped delay line (TDL) model is adopted in the CIR simulation. In Figure 5, it can be clearly seen that the locations of different clusters change with time. It needs to be mentioned that the reality scenario is more complicated, since the power of the ray is constantly changing, and new scatterers will appear that accompany existed scatterers' disappearance.

In Figure 6, we give a snapshot of the TDL at $t = 5$ s. It can be seen that due to the setting of Tx, Rx, and other vehicles' velocities and locations, different clusters gather together after a certain period of time.

5.2. Spatial ACF. This part is the simulation result of spatial ACF. Figure 7 shows the spatial ACFs of scenarios with and without slope at Tx end. The spacing between the two receiving antennas at Rx is fixed, and the antenna spacing in Figure 7 refers to the spacing between adjacent transmitting antennas at Tx. For example, in our simulation, there are $N_c = 4$ clusters of scatterers around the Tx and Rx, respectively, and each clusters contains 10 effective scatterers ($N_{i_1} = N_{j_2} = 10$). Since there are at total $N_c \times N_{i_1} \times N_c \times N_{j_2}$ DB paths, the spatial diversity is huge. As a result, the spatial ACF of the channel is therefore relatively low.

Figure 7 presents normalized spatial ACFs for scenarios including slope with different tilt angles, i.e., $\theta_{\mathrm{slope}} = 0$, $\theta_{\mathrm{slope}} = \pi/36$, $\theta_{\mathrm{slope}} = \pi/6$, and $\theta_{\mathrm{slope}} = \pi/3$. The figure shows that the tilt angle of the slope has little effect on the spatial ACF. As the tilt angle of slope increases, the main lobe of the spatial ACF becomes narrower.

5.3. Temporal ACF

5.3.1. The ACF at Initial Time. When simulating the temporal ACF, it is necessary to, respectively, fix the spacing of adjacent transmitting and receiving antennas at Tx and Rx. We take $\delta_T = \delta_R = \lambda$ in the simulations. The generation of

Table 2: Simulation parameters.

Parameter	Value	
	Scenario without slope	Scenario with slope
f_c	5.9 GHz	5.9 GHz
K	3.786	3.786
k	15	15
D	200 m	
(D_1, D_2)		(100, 100) m
(R_T, R_R)	((15, 20), (15, 20)) m	((15, 20), (15, 20)) m
(δ_T, δ_R)	(λ, λ)	(λ, λ)
(v_T, v_R)	(30, 40) m/s	(30, 40) m/s
$v_{\text{scatterer}}$	35 m/s	35 m/s
(ϕ_T, ϕ_R)	(0, 0) rad	(0, 0.08) rad
(γ_T, γ_R)	(0, 0) rad	(0, 0) rad
$(f_{T_{\max}}, f_{R_{\max}})$	(590, 787) Hz	(590, 787) Hz
(θ_T, θ_R)	(1.57, 1.57) rad	(1.57, 1.57) rad
$\alpha_T^{(n_{ij})}$	(−2.36, −0.76, 0.76, 2.36) rad	(−2.36, −0.76, 0.76, 2.36) rad
$\alpha_R^{(n_{ij})}$	(−2.36, −0.76, 0.76, 2.36) rad	(−2.36, −0.76, 0.76, 2.36) rad
$\beta_T^{(n_{ij})}$	(0, 0, 0, 0) rad	(0, 0, 0, 0) rad
$\beta_R^{(n_{ij})}$	(0, 0, 0, 0) rad	(−0.07, 0.07, 0.07, −0.07) rad
$(\alpha_T^{\text{LoS}}, \beta_T^{\text{LoS}})$	(0, 0) rad	(0, 0.06) rad
$(\alpha_R^{\text{LoS}}, \beta_R^{\text{LoS}})$	(3.14, 0) rad	(3.14, −0.06) rad
N_c	4	4
N_{i_1}, N_{i_2}	(10, 10)	(10, 10)
θ_{slope}		0.08 rad

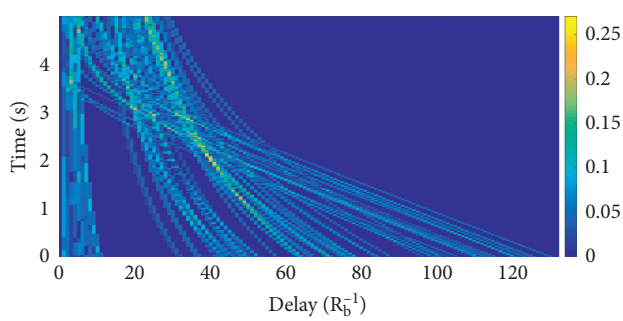

Figure 5: The normalized TDL model without the LoS component.

the scatterers is the same as that in the simulation of the spatial ACF. The specific results are shown in Figure 8.

In the VMF distribution, the number of α_0 is $2 \times N_c$ because there are N_c clusters of scatters near Tx and another N_c clusters of scatters near Rx, the values of them are listed in Table 2, and the values of β_0 are set to zero.

Figure 8 shows the temporal ACFs for scenarios with a slope of different tilt angles, and the angles are the same as above. It can be seen from the figure that as the tilt angle of slope increases, the main lobe of the temporal ACF becomes wider.

5.3.2. Time-Varying ACF. In this simulation, we assume that the speeds of the Tx, Rx, and vehicles around them are 30 m/s, 40 m/s, and 35 m/s, respectively. The results of the simulation are shown in Figures 9 and 10.

From Figure 9, we can observe the nonstationary feature of the channel. It also verifies that when the speed directions of Tx and Rx coincide, the channel can be regarded as a stationary channel in a short interval (within 1 second). Figure 10 illustrates more detailed time-variant features of the ACFs at different moments, e.g., at the moments $t = 0$ s, 1 s, 3 s, and 5 s. In the simulated scenario set, different vehicles are moving away from each other as time increases. Therefore, the different scattering paths are constantly moving closer together, as shown in Figure 11, the AAoA of SB_1 becomes closer to the LoS path (0 radians). And the difference between the angles of the scattering paths and the delays are continuously decreasing. Eventually, it leads to an increase in the main lobe of the ACF.

5.4. Doppler PSD. The simulated Doppler PSDs are shown in Figures 12 and 13. The result of Figure 12 is consistent with Figure 5. As time increases, Tx and Rx keep moving away from each other, and different clusters gather with each other. It results in a decrease in the width of Doppler frequency.

We have $N_{i_1} = N_{j_2} = 10$, so there should be a total of N clusters of impulses in Figure 13, i.e., $N = N_1 + N_2 + N_3$, $N_1 = N_c \times N_{i_1}$ and $N_2 = N_c \times N_{j_2}$, $N_3 = N_c \times N_{i_1} \times N_c \times N_{j_2}$. However, in Figure 13, only $N_1 + N_2$ clusters of SB path impulses can be seen because the energy of DB path is too low. Furthermore, in each cluster of scatterers, all scatterers are surrounding the same direction, so as it can be seen in Figure 13 that these impulses are in the form of clusters. Besides, the Doppler PSD provides help to verify the correctness of the model. After comparison and verification, the Doppler PSDs shown in Figures 12 and 13 are consistent with the theoretical analysis.

5.5. Comparison with Measurements. In this section, we compare the simulation results of the model with measurement data to verify the accuracy of the model. We choose the parameter and fitting cure given in [52] and adjust the vehicle's distribution and movement in the model to match the measurement scenario. After adjusting the model, we simulate RMS delay spread, RMS Doppler spread, and RMSE to be compared with the measurement data.

5.5.1. Adjustments of Scenario. The adjusted scenario is shown in Figure 14. Since the measurement environments are level roads, we set the tilt angle of slope to zero. At the initial time, Tx and Rx are moving on two adjacent lanes, then Rx accelerates and overtakes Tx. The velocity of different vehicles varies according to different scenarios.

In [52], measurement campaigns are in four different scenarios, highway, urban, suburb, and municipal lake. In the lake scenario, there is very little scattering caused by the environment because there are almost no buildings in this scenario, and the small-scale fading of the channel mainly comes from the scattering caused by the surrounding vehicles. In other measurement scenarios, the environment causes severe channel fading. Therefore, we added

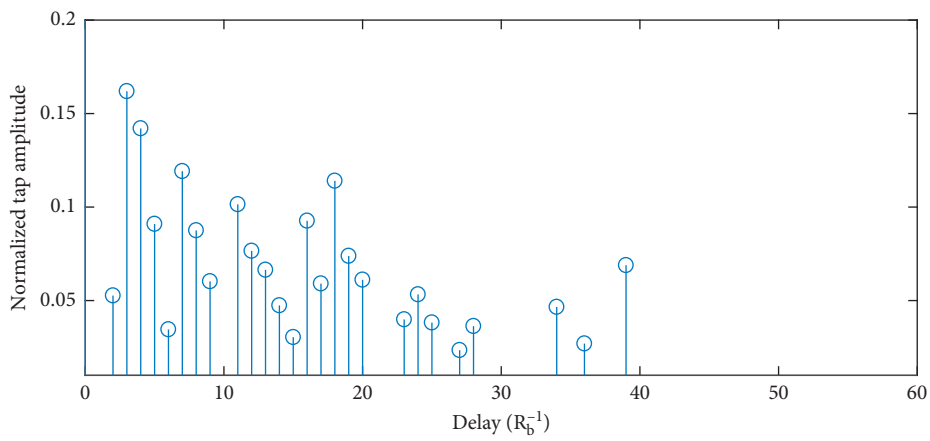

Figure 6: A snapshot of the TDL model at $t = 5$ s.

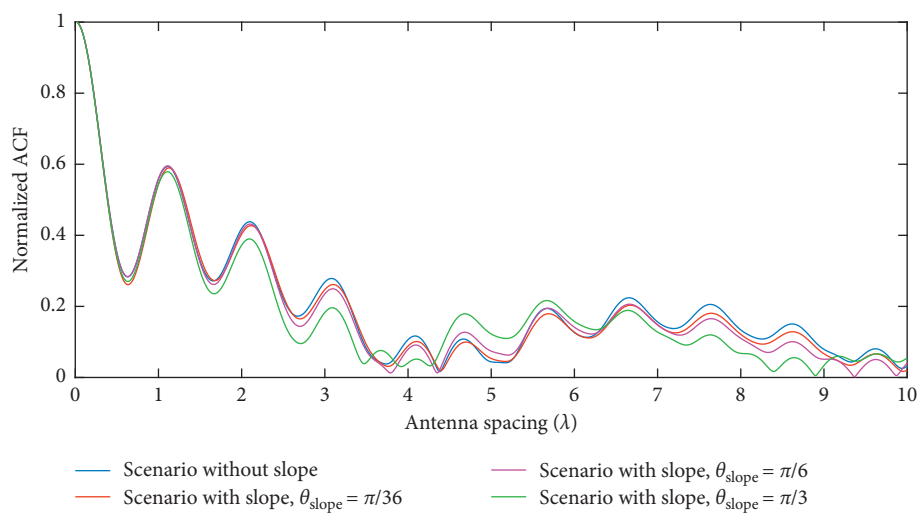

Figure 7: Spatial ACFs for the 3D model with and without slope.

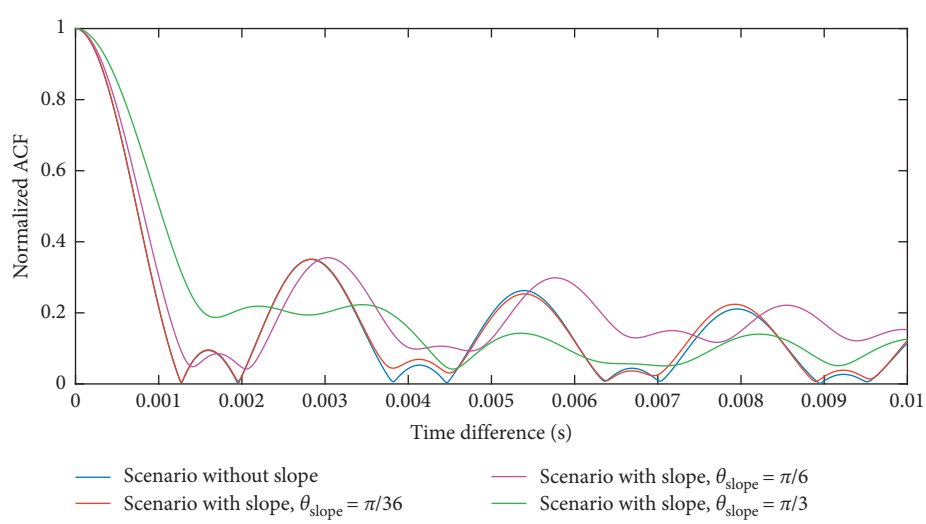

Figure 8: Temporal ACF for the 3D model with and without slope.

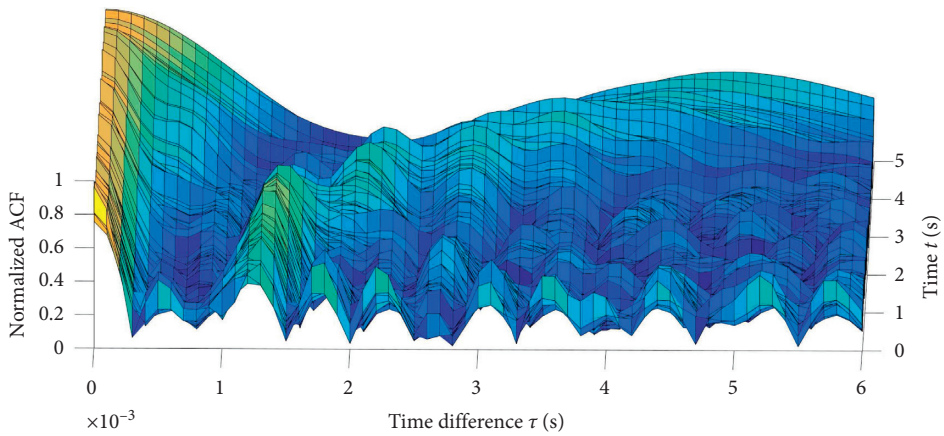

Figure 9: Time-varying ACF for the 3D model.

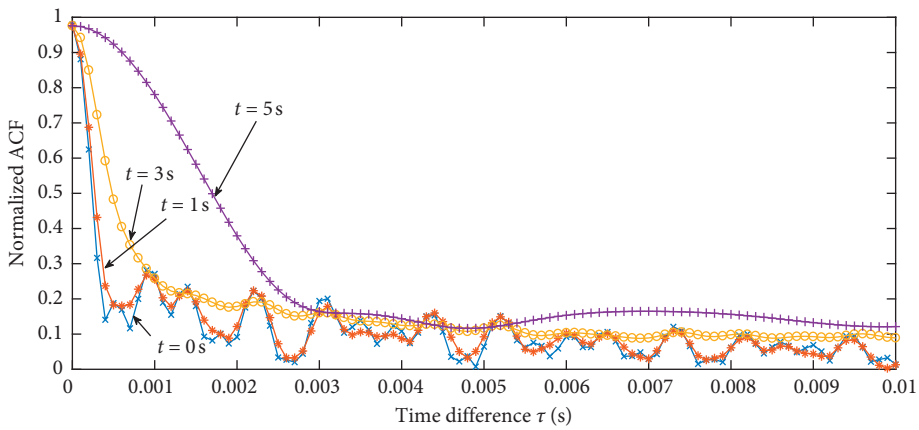

Figure 10: ACF at $t = 0$ s, 1 s, 3 s, and 5 s for the 3D model.

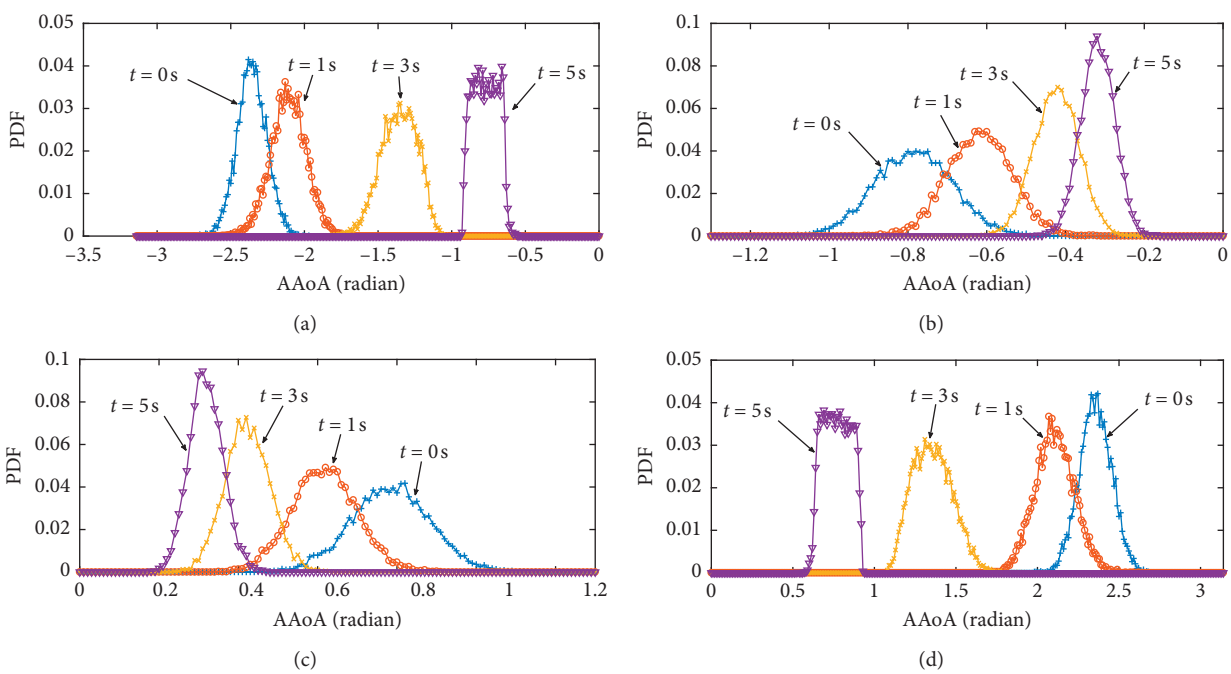

Figure 11: The pdf of AAoA of (a)cluster$_1$, (b)cluster$_2$, (c)cluster$_3$, and (d)cluster$_4$ SB$_1$ path at $t = 0$, 1, 3, and 5 s.

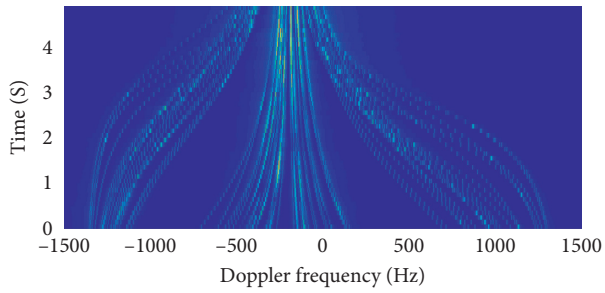

Figure 12: Doppler PSD for the 3D model.

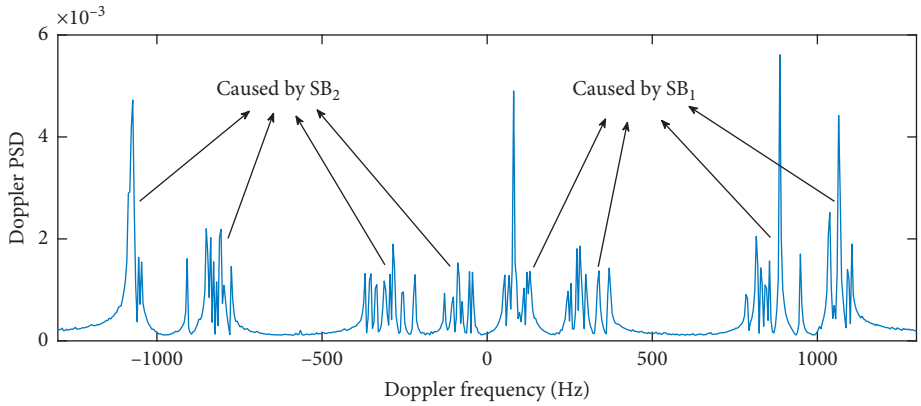

Figure 13: Doppler PSD for the 3D model at $t = 0$ s.

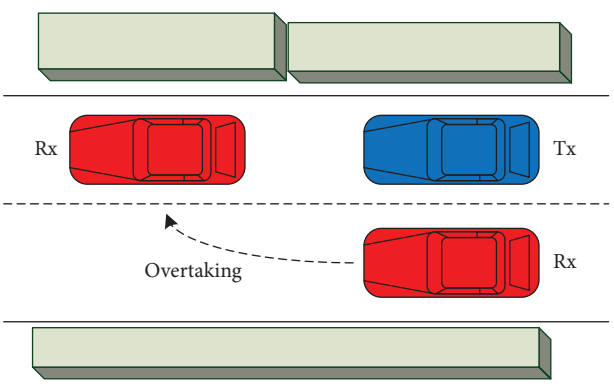

Figure 14: Adjusted scenario.

environment scatterers in the simulation. The distribution of environment scatterers varies according to the scenario. In suburb and urban scenarios, the environment scatterers are distributed on both sides of the lane. The main difference is that there are dense trees on both sides of the road in suburb areas, as for urban areas, there are mainly dense large buildings on both sides of the lane. In the highway scenario, the environment scatterers are only distributed on one side, and they are mainly sparse houses.

Besides, it can be divided into overtaking (OT) and nonovertaking (NOT) cases according to the distance between Tx and Rx. In the case of OT, the distance between Tx and Rx is very close, less than 11 m. While in the NOT case, they keep a certain distance.

5.5.2. RMS Delay Spread. In wireless communication, RMS delay spread is a statistical parameter that can describe the delay characteristics of the radio channel. It is often used in the evaluation of channel characteristics. In V2V communication, the multipath effect caused by the scattering between vehicles and scattering from the environment caused small-scale fading. RMS delay spread can reflect this multipath effect.

The complex time-varying CIR can be derived by an inverse Fourier transform of the channel transfer function (6a)–(6c). Then, we can calculate the time-variant power delay profile (PDP) by averaging the magnitude squared of the CIR.

$$P(t,\tau) = |h(t,\tau)|^2 = \sum_i |a_i(t)|^2 \delta(\tau - \tau_i), \tag{17}$$

where a_i is the complex coefficient of each delay path, and τ_i is the excess delay of the ith path.

Then, we can get the RMS delay T_{rms} as follows:

$$T_m = \frac{1}{\int_{-\infty}^{\infty} P_A(\tau)\mathrm{d}\tau} \cdot \int_{-\infty}^{\infty} P_A(\tau)\tau \mathrm{d}\tau, \tag{18a}$$

$$T_{\text{rms}} = \sqrt{\frac{1}{\int_{-\infty}^{\infty} P_A(\tau)\mathrm{d}\tau} \cdot \int_{-\infty}^{\infty} P_A(\tau)\tau^2 \mathrm{d}\tau - T_m^2}, \tag{18b}$$

where $P_A(\tau)$ is the averaged power delay profile.

The comparison results are shown in Figure 15. The fitting curves corresponding to different scenarios are given

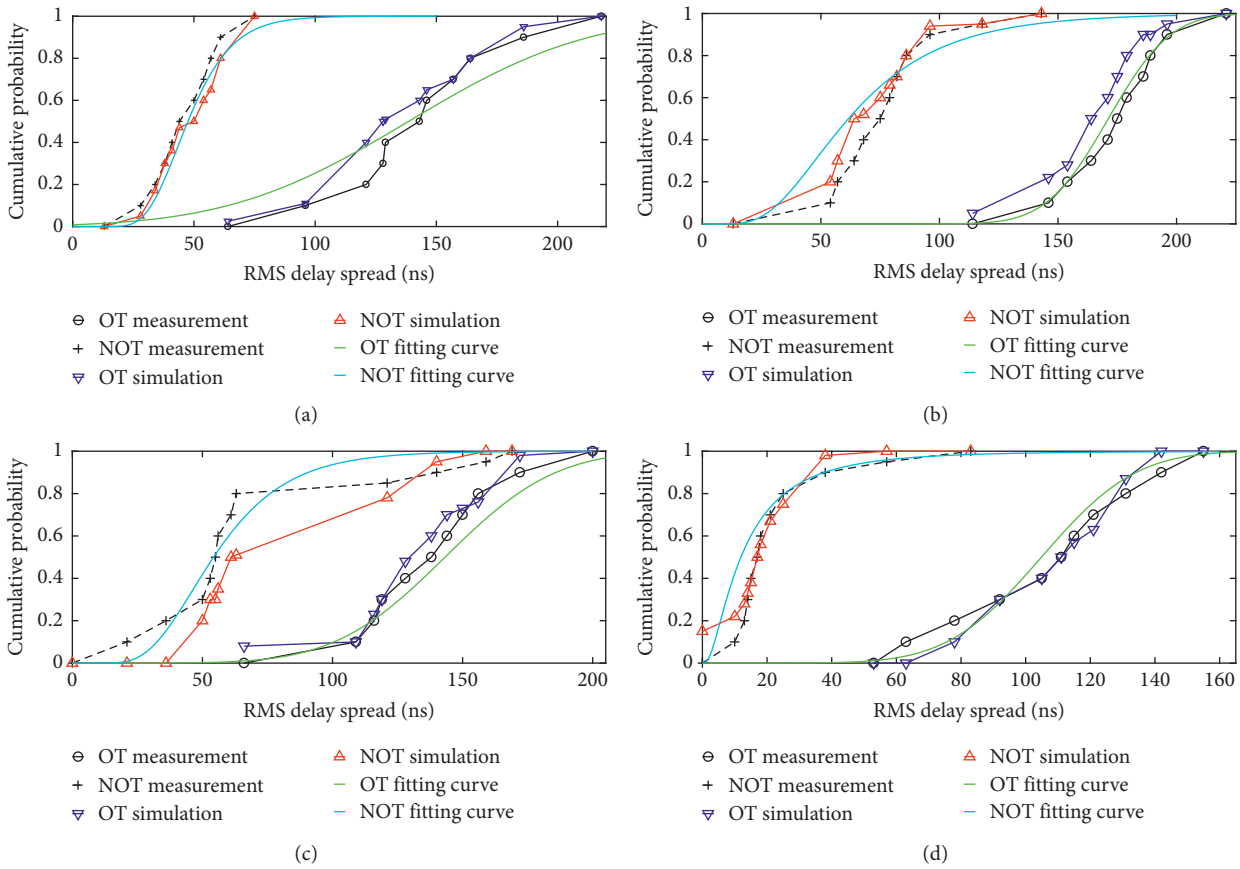

Figure 15: The CDF of RMS delay spread for (a) highway, (b) urban, (c) suburb, and (d) municipal lake scenario.

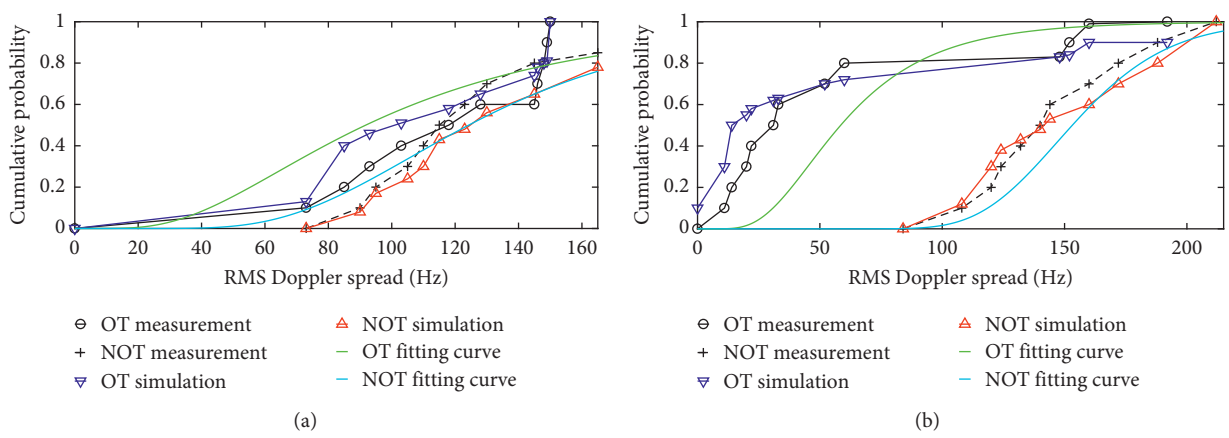

Figure 16: Continued.

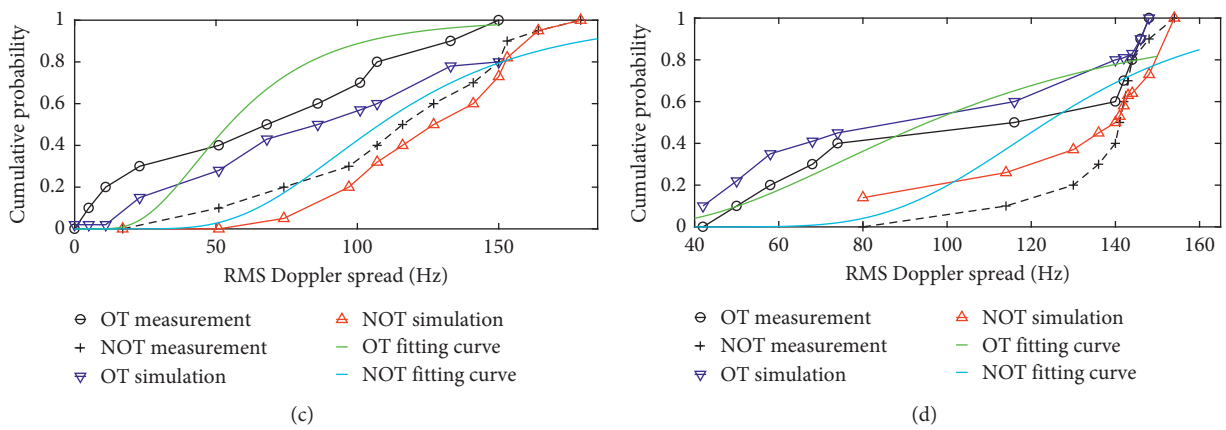

Figure 16: The CDF of RMS Doppler spread for (a) highway, (b) urban, (c) suburb, and (d) municipal lake scenario.

Table 3: Data of RMSE.

Scenario	Highway		Urban		Suburb		Lake	
Case	OT	NOT	OT	NOT	OT	NOT	OT	NOT
Delay RMSE between simulation result and measurement data								
RMSE	0.0990	0.0729	0.1464	0.0864	0.0622	0.1535	0.0608	0.0698
Delay RMSE between fitting distribution and measurement data								
RMSE	0.1058	0.0701	0.0476	0.1516	0.0816	0.0847	0.0668	0.1743
Difference of delay RMSE								
RMSE	−0.0068	0.0028	0.0988	−0.0652	−0.0193	0.0688	−0.0059	−0.1044
Doppler RMSE between simulation result and measurement data								
RMSE	0.1007	0.0901	0.1463	0.0694	0.1356	0.0867	0.1064	0.1233
Doppler RMSE between fitting distribution and measurement data								
RMSE	0.1660	0.0988	0.2545	0.1238	0.1503	0.0720	0.1061	0.2210
Difference of Doppler RMSE								
RMSE	−0.0653	−0.0087	−0.1082	−0.0544	−0.0146	0.0147	0.0003	−0.0977

in [52]. We put simulation results, measurement data, and fitting curves together for comparison. In the following section, RMSE will be used for evaluation.

5.5.3. RMS Doppler Spread. In V2V communication, vehicles are moving at high speed, and the speed direction of vehicles may change, so it causes a strong Doppler effect. Therefore, RMS Doppler spread is also applied to the description of V2V channel delay characteristics.

We can get the RMS Doppler spread D_{rms} as

$$P_{Bm} = \int_{-\infty}^{\infty} P_B(\nu)\mathrm{d}\nu, \tag{19a}$$

$$D_m = \frac{\int_{-\infty}^{\infty} P_B(\nu)\nu\mathrm{d}\nu}{P_{Bm}}, \tag{19b}$$

$$D_{\text{rms}} = \sqrt{\frac{\int_{-\infty}^{\infty} P_B(\nu)\nu^2\mathrm{d}\nu}{P_{Bm}} - D_m^2}, \tag{19c}$$

where P_{Bm} represents the integration of scattering function.

The comparison results are shown in Figure 16. The comparison of simulation results, measurement data, and fitting curves are given in the figure.

5.5.4. RMSE. To verify that the model can fit the measurement data better than the fitting curve, we calculate the RMSE of delay and Doppler spread.

$$\text{RMSE} = \sqrt{\frac{1}{n}\sum_{i=1}^{n}(x_i - y_i)^2}, \tag{20}$$

where y_i denotes the measurement data, and x_i denotes the simulation result or the fitting curve.

RMSE can reflect the fitting degree of simulation results and measurement data. A smaller RMSE means a better fitting. The calculation results are shown in Table 3. When the difference of RMSE is negative, it indicates that the model can better fit the measurement data than the fitting curve. As can be seen in the table, the model has a smaller RMSE in most cases, and the model has a similar degree to the fitting curve in the remaining scenarios.

6. Conclusion

In this study, we developed an analytical multicluster nonstationary 3D MIMO channel model for the V2V communication system, which is suitable for the scenario where there are a certain number of vehicles near Tx and Rx on or near a slope. After simplification, the model can be applied to the normal road without slope. In addition, we also considered the impact of vehicle changing lanes. Furthermore, we derived and simulated statistical properties of the proposed channel such as the spatial ACF, temporal ACF, time-varying ACF, and Doppler PSD. Finally, we compared the simulation results with the measurement data in four scenarios. The comparison results show that the proposed model can mimic the measurement data better than the fitting curve. These simulation results have shown the utility of the proposed model.

Data Availability

The data used to support the findings of this study are available from the corresponding author upon request.

Conflicts of Interest

The authors declare that they have no conflicts of interest.

Acknowledgments

The authors would like to express their appreciation to Professor Hongwen Yang from the Beijing University of Posts and Telecommunications for his help and advice.

References

[1] A. M. Vegni and V. Loscrí, "A survey on vehicular social networks," *IEEE Communications Surveys & Tutorials*, vol. 17, no. 4, pp. 2397–2419, 2015.

[2] K. Zheng, Q. Zheng, P. Chatzimisios, W. Xiang, and Y. Zhou, "Heterogeneous vehicular networking: a survey on architecture, challenges, and solutions," *IEEE Communications Surveys & Tutorials*, vol. 17, no. 4, pp. 2377–2396, 2015.

[3] G. Karagiannis, O. Altintas, E. Ekici et al., "Vehicular networking: a survey and tutorial on requirements, architectures, challenges, standards and solutions," *IEEE Communications Surveys & Tutorials*, vol. 13, no. 4, pp. 584–616, 2011.

[4] E. Ahmed and H. Gharavi, "Cooperative vehicular networking: a survey," *IEEE Transactions on Intelligent Transportation Systems*, vol. 19, no. 3, pp. 996–1014, 2018.

[5] P. Papadimitratos, A. La Fortelle, K. Evenssen, R. Brignolo, and S. Cosenza, "Vehicular communication systems: enabling technologies, applications, and future outlook on intelligent transportation," *IEEE Communications Magazine*, vol. 47, no. 11, pp. 84–95, 2009.

[6] L. Liang, H. Peng, G. Y. Li, and X. Shen, "Vehicular communications: a physical layer perspective," *IEEE Transactions on Vehicular Technology*, vol. 66, no. 12, pp. 10647–10659, 2017.

[7] P. Almers, E. Bonek, A. Burr et al., "Survey of channel and radio propagation models for wireless MIMO systems," *EURASIP Journal on Wireless Communications and Networking*, vol. 2007, no. 1, Article ID 19070, 2007.

[8] F. Rusek, D. Persson, B. K. Lau, E. G. Larsson, T. L. Marzetta, and F. Tufvesson, "Scaling up MIMO: opportunities and challenges with very large arrays," *IEEE Signal Processing Magazine*, vol. 30, no. 1, pp. 40–60, 2013.

[9] T. Ohira, T. Hirai, S. Tomisato, and M. Hata, "A study of mobile path loss estimation models for a sloping terrain area in cellular systems," in *Proceedings of the 18th Asia-Pacific Conference on Communications (APCC 2012)*, pp. 472–477, Jeju, Korea, October 2012.

[10] M. Nisirat, M. Ismail, L. Nissirat, and S. Al Khawaldeh, "Micro cell path loss estimation by means of terrain slope for 900 and 1800 MHz," in *Proceedings of the International Conference on Computer and Communication Engineering*, pp. 670–674, Kuala Lumpur, Malaysia, July 2012.

[11] Z. H. Mir and F. Filali, "Simulation and performance evaluation of vehicle-to-vehicle (V2V) propagation model in urban environment," in *Proceedings of the 2016 7th International Conference on Intelligent Systems, Modelling and Simulation (ISMS)*, Bangkok, Thailand, January 2016.

[12] Q. Zhu, W. Li, C.-X. Wang et al., "Temporal correlations for a non-stationary vehicle-to-vehicle channel model allowing velocity variations," *IEEE Communications Letters*, vol. 23, no. 7, pp. 1280–1284, 2019.

[13] G. Acosta and M. A. Ingram, "Six time- and frequency-selective empirical channel models for vehicular wireless LANs," *IEEE Vehicular Technology Magazine*, vol. 2, no. 4, pp. 4–11, 2007.

[14] X. Cheng, C.-X. Wang, Y. Yuan, D. I. Laurenson, and X. Ge, "A novel 3D regular-shaped geometry-based stochastic model for non-isotropic MIMO mobile-to-mobile channels," in *Proceedings of the 2010 IEEE 72nd Vehicular Technology Conference-Fall*, pp. 1–5, Ottawa, Canada, September 2010.

[15] J. Karedal, F. Tufvesson, N. Czink et al., "A geometry-based stochastic MIMO model for vehicle-to-vehicle communications," *IEEE Transactions on Wireless Communications*, vol. 8, no. 7, pp. 3646–3657, 2009.

[16] L. Jiang and S. Y. Tan, "Geometrically based statistical channel models for outdoor and indoor propagation environments," *IEEE Transactions on Vehicular Technology*, vol. 56, no. 6, pp. 3587–3593, 2007.

[17] J. Zhou, H. Jiang, and H. Kikuchi, "Generalised three-dimensional scattering channel model and its effects on compact multiple-input and multiple-output antenna receiving systems," *IET Communications*, vol. 9, no. 18, pp. 2177–2187, 2015.

[18] A. S. Akki, "Statistical properties of mobile-to-mobile land communication channels," *IEEE Transactions on Vehicular Technology*, vol. 43, no. 4, pp. 826–831, 1994.

[19] X. Liang, X. Zhao, Y. Li, S. Li, and Q. Wang, "A non-stationary geometry-based street scattering model for vehicle-to-vehicle wideband MIMO channels," *Wireless Personal Communications*, vol. 90, no. 1, pp. 325–338, 2016.

[20] H. Jiang, Z. Zhang, J. Dang, and L. Wu, "A novel 3-D massive MIMO channel model for vehicle-to-vehicle communication environments," *IEEE Transactions on Communications*, vol. 66, no. 1, pp. 79–90, 2018.

[21] A. Paier, L. Bernado, J. Karedal, O. Klemp, and A. Kwoczek, "Overview of vehicle-to-vehicle radio channel measurements for collision avoidance applications," in *Proceedings of the 2010 IEEE 71st Vehicular Technology Conference (VTC-Spring)*, pp. 1–5, Taipei, Taiwan, May 2010.

[22] T. Abbas, J. Nuckelt, T. Kürner, T. Zemen, C. F. Mecklenbräuker, and F. Tufvesson, "Simulation and measurement-based vehicle-to-vehicle channel

characterization: accuracy and constraint analysis," *IEEE Transactions on Antennas and Propagation*, vol. 63, no. 7, pp. 3208–3218, 2015.

[23] C. Li, K. Yang, J. Yu et al., "V2V radio channel performance based on measurements in ramp scenarios at 5.9 GHz," *IEEE Access*, vol. 6, pp. 7503–7514, 2018.

[24] A. Ghazal, C.-X. Wang, B. Ai, D. Yuan, and H. Haas, "A non-stationary wideband MIMO channel model for high-mobility intelligent transportation systems," *IEEE Transactions on Intelligent Transportation Systems*, vol. 16, no. 2, pp. 885–897, 2015.

[25] A. G. Zajic and G. L. Stuber, "Space-time correlated mobile-to-mobile channels: modelling and simulation," *IEEE Transactions on Vehicular Technology*, vol. 57, no. 2, pp. 715–726, 2008.

[26] A. G. Zajic and G. L. Stuber, "Three-dimensional modeling, simulation, and capacity analysis of space-time correlated mobile-to-mobile channels," *IEEE Transactions on Vehicular Technology*, vol. 57, no. 4, pp. 2042–2054, 2008.

[27] X. Cheng, C.-X. Wang, D. Laurenson, S. Salous, and A. Vasilakos, "An adaptive geometry-based stochastic model for non-isotropic MIMO mobile-to-mobile channels," *IEEE Transactions on Wireless Communications*, vol. 8, no. 9, pp. 4824–4835, 2009.

[28] Y. Yuan, C.-X. Wang, X. Cheng, B. Ai, and D. I. Laurenson, "Novel 3D geometry-based stochastic models for non-isotropic MIMO vehicle-to-vehicle channels," *IEEE Transactions on Wireless Communications*, vol. 13, no. 1, pp. 298–309, 2014.

[29] H. Jiang, Z. Zhang, L. Wu, and J. Dang, "Novel 3-D irregular-shaped geometry-based channel modeling for semi-ellipsoid vehicle-to-vehicle scattering environments," *IEEE Wireless Communications Letters*, vol. 7, no. 5, pp. 836–839, 2018.

[30] M. Riaz, S. J. Nawaz, and N. M. Khan, "3D ellipsoidal model for mobile-to-mobile radio propagation environments," *Wireless Personal Communications*, vol. 72, no. 4, pp. 2465–2479, 2013.

[31] S. J. Nawaz, M. Riaz, N. M. Khan, and S. Wyne, "Temporal analysis of a 3D ellipsoid channel model for the vehicle-to-vehicle communication environments," *Wireless Personal Communications*, vol. 82, no. 3, pp. 1337–1350, 2015.

[32] M. Riaz, N. M. Khan, and S. J. Nawaz, "A generalized 3-D scattering channel model for spatiotemporal statistics in mobile-to-mobile communication environment," *IEEE Transactions on Vehicular Technology*, vol. 64, no. 10, pp. 4399–4410, 2015.

[33] W. I. Waseer, S. Junaid Nawaz, S. M. Gulfam, and M. J. Mughal, "Second-order fading statistics of massive-MIMO vehicular radio communication channels," *Transactions on Emerging Telecommunications Technologies*, vol. 29, no. 10, Article ID e3487, 2018.

[34] Y. Li, R. He, S. Lin et al., "Cluster-based nonstationary channel modeling for vehicle-to-vehicle communications," *IEEE Antennas and Wireless Propagation Letters*, vol. 16, pp. 1419–1422, 2017.

[35] D. Du, X. Zeng, X. Jian, L. Miao, and H. Wang, "Three-Dimensional Vehicle-to-vehicle channel modeling with multiple moving scatterers," *Mobile Information System*, vol. 2017, pp. 1–14, 2017.

[36] X. Cheng, Q. Yao, M. Wen, C. Wang, L. Song, and B. Jiao, "Wideband channel modeling and intercarrier interference cancellation for vehicle-to-vehicle communication systems," *IEEE Journal on Selected Areas in Communications*, vol. 31, no. 9, pp. 434–448, 2013.

[37] Y. Yuan, C.-X. Wang, Y. He, M. M. Alwakeel, and E.-H. M. Aggoune, "3D wideband non-stationary geometry-based stochastic models for non-isotropic MIMO vehicle-to-vehicle channels," *IEEE Transactions on Wireless Communications*, vol. 14, no. 12, pp. 6883–6895, 2015.

[38] H. Jiang, Z. Zhang, L. Wu, and J. Dang, "A non-stationary geometry-based scattering vehicle-to-vehicle MIMO channel model," *IEEE Communications Letters*, vol. 22, no. 7, pp. 1510–1513, 2018.

[39] Y. Liu, Z. Tan, and X. Chen, "Modeling the channel time variation using high-order-motion model," *IEEE Communications Letters*, vol. 15, no. 3, pp. 275–277, 2011.

[40] X. Cheng, C.-X. Wang, B. Ai, and H. Aggoune, "Envelope level crossing rate and average fade duration of nonisotropic vehicle-to-vehicle Ricean fading channels," *IEEE Transactions on Intelligent Transportation Systems*, vol. 15, no. 1, pp. 62–72, 2014.

[41] A. G. Zaji, G. L. Stuber, T. G. Pratt, and S. Son Nguyen, "Statistical modelling and experimental verification for wideband MIMO mobile-to-mobile channels in urban environments," in *Proceedings of the 2008 International Conference on Telecommunications*, pp. 1–6, St. Petersburg, Russia, January 2008.

[42] A. Theodorakopoulos, P. Papaioannou, T. Abbas, and F. Tufvesson, "A geometry based stochastic model for mimo v2v channel simulation in cross-junction scenario," in *Proceedings of the 2013 13th International Conference on ITS Telecommunications (ITST)*, pp. 290–295, Tampere, Finland, November 2013.

[43] S. Wu, C.-X. Wang, E.-H. M. Aggoune, M. M. Alwakeel, and Y. He, "A non-stationary 3-D wideband twin-cluster model for 5G massive MIMO channels," *IEEE Journal on Selected Areas in Communications*, vol. 32, no. 6, pp. 1207–1218, 2014.

[44] J. Bian, C.-X. Wang, J. Huang et al., "A 3D wideband non-stationary multi-mobility model for vehicle-to-vehicle MIMO channels," *IEEE Access*, vol. 7, pp. 32562–32577, 2019.

[45] K. Mammasis, R. W. Stewart, and J. S. Thompson, "Spatial fading correlation model using mixtures of von Mises Fisher distributions," *IEEE Transactions on Wireless Communications*, vol. 8, no. 4, pp. 2046–2055, 2009.

[46] K. Mammasis, P. Santi, and A. Goulianos, "A three-dimensional angular scattering response including path powers," *IEEE Transactions on Wireless Communications*, vol. 11, no. 4, pp. 1321–1333, 2012.

[47] Y. Bi, J. Zhang, M. Zeng, M. Liu, and X. Xu, "A novel 3D nonstationary channel model based on the von Mises-Fisher scattering distribution," *Mobile Information Systems*, vol. 2016, p. 1, Article ID e2161460, 2016.

[48] Q. Zhu, Y. Yang, X. Chen et al., "A novel 3D non-stationary vehicle-to-vehicle channel model and its spatial-temporal correlation properties," *IEEE Access*, vol. 6, pp. 43633–43643, 2018.

[49] L. Pengyu, D. W. Matolak, A. Bo, and S. Ruoyu, "Path loss modeling for vehicle-to-vehicle communication on a slope," *IEEE Transactions on Vehicular Technology*, vol. 63, no. 6, pp. 2954–2958, 2014.

[50] S. Wu, C.-X. Wang, E.-H. M. Aggoune, M. M. Alwakeel, and X. You, "A general 3-D non-stationary 5G wireless channel model," *IEEE Transactions on Communications*, vol. 66, no. 7, pp. 3065–3078, 2018.

[51] G. D. Durgin and T. S. Rappaport, "Theory of multipath shape factors for small-scale fading wireless channels," *IEEE Transactions on Antennas and Propagation*, vol. 48, no. 5, pp. 682–693, 2000.

[52] C. Fuxing, C. Wei, Y. Junyi, L. Changzhen, and L. fang, "Vehicle-to-vehicle propagation channel performance for overtaking cases based on measurements," *IEEE Access*, vol. 7, pp. 150327–150338, 2019.

[53] A. Paier, T. Zemen, L. Bernado et al., "Non-WSSUS vehicular channel characterization in highway and urban scenarios at 5.2 GHz using the local scattering function," in *Proceedings of the 2008 International ITG Workshop on Smart Antennas*, Vienna, Austria, March 2008.

[54] Y. Shui, F. Li, J. Yu et al., "Vehicle-to-vehicle radio channel characteristics for congestion scenario in dense urban region at 5.9 GHz," *International Journal of Antennas and Propagation*, vol. 2018, pp. 1–14, 2018.

[55] D. Vlastaras, T. Abbas, M. Nilsson, R. Whiton, M. Olbäck, and F. Tufvesson, "Impact of a truck as an obstacle on vehicle-to-vehicle communications in rural and highway scenarios," in *Proceedings of the 2014 IEEE 6th International Symposium on Wireless Vehicular Communications (WiVeC 2014)*, pp. 1–6, Vancouver, BC, Canada, September 2014.